

INTERACTION OF LASER RADIATION WITH MATTER. LASER PLASMA https://doi.org/10.1070/QEL17555

X-ray production and charged-particle acceleration in the irradiation of micro- and nanorod arrays by high-power femtosecond laser pulses

K.A. Ivanov, I.M. Mordvintsev, Yu.V. Kargina, S.A. Shulyapov, I.N. Tsymbalov, I.V. Bozhev, R.V. Volkov, V.Yu. Timoshenko, A.B. Savel'ev

Abstract. **The effect of the size of the rods at the structured silicon target surface on the parameters of the plasma produced when the target is exposed to a high-contrast femtosecond laser pulse with an intensity of 2×10^{18} W cm^{-2} is investigated. It is shown that irradiation of a target with subwavelength rods (~100 nm in diameter) provides a significant (up to 250 keV) increase in the temperature of hot plasma electrons and their number in comparison with those obtained in the case of a plane target. It was found that in this case the yield of hard X-ray radiation increases several-fold. The observed effect can be attributed to increased absorption and particle motion in a complex field near plasma nonuniformities. It is shown that the presence of rods with a characteristic size of ~1 μm promotes an increase in the production efficiency of multiply charged silicon ions. The result obtained is apparently associated with the radiation penetration between the rods and with collisional ionisation of particles as they fly into vacuum from deeper target layers.**

Keywords: *relativistic laser-produced plasma, microrods, nanorods, electron acceleration, X-ray radiation, fast ions.*

1. Introduction

Various sources of radiation and charged particles based on the interaction of ultrashort relativistically intense (over 10^{18} W cm^{-2}) laser radiation with plasma [1, 2] have broad prospects in the solution of fundamental and applied problems. These are X-ray diagnostics with subpicosecond time resolution (studies of shock waves in plasmas [3], time-resolved X-ray spectroscopy [4], phase-contrast measurements [5]), production of fast electron [6] and ion [7] beams, initiation of nuclear reactions [8, 9], high energy density physics [10], and nuclear photonics [11]. At the same time, the compactness and relatively low cost of multi-terawatt laser systems capable of providing the required interaction regime open up the possibility of conducting research in different fields of science and technology.

To improve the conversion efficiency of laser energy to the energy of generated particles and photons, several approaches were developed, including controlling preplasma length with prepulses [12, 13], using low-density targets [14], as well as using targets on whose surfaces are structures with a small characteristic size of the elements (down to nanometre-scale structures). The last-named approach turned out to be highly efficient for 'moderate', subrelativistic intensities [15–17], and it is actively investigated in the relativistic interaction regime in terms of increasing the X-ray photon flux from the plasma [18, 19], increasing the electron energy in it [20, 21], and a more efficient ion acceleration [22, 23]. An important factor is also the development of the methods of structure growth on the surfaces of different materials by electrochemical etching [24], laser ablation [25], etc.

The use of structured targets imposes stringent requirements on the contrast of a laser pulse: the ratio of the intensity of the main pulse to the intensity of amplified spontaneous emission (ASE) pedestal or to the intensities of prepulses that inevitably appear during amplification of chirped pulses, since the effect of sufficiently intense prepulses of various types can lead to heating and partial ablation of the structures or even to their destruction. In this case, the melting and ablation thresholds of the structured target surface are lower than those of a target with a flat surface, due to the limitation of the heat outflow into the depth of the target and the enhanced absorption of laser radiation energy [26, 27]. Moreover, this decrease naturally depends on the surface morphology: structures with larger elements are less sensitive to the deterioration of the contrast of laser radiation.

Surface morphology also has a significant effect on the absorption of laser radiation, acceleration of electrons, etc. [23, 28, 29]. In particular, the effects of local field enhancement on submicron structures [18, 19], stochastic motion of particles in complex fields formed by laser radiation and quasi-static fields of the structures themselves [28, 30] lead to an increase in the number of accelerated electrons in the plasma and to an increase in their energy. Numerical studies revealed that subwavelength structures offer certain advantages in this case [18, 31]. At the same time, larger structures provide the penetration of radiation into the gaps between them, which leads to heating of a thicker surface layer [32] and to the manifestation of plasmon effects and resonances [33, 34].

K.A. Ivanov, I.M. Mordvintsev Lebedev Physical Institute, Russian Academy of Sciences, Leninsky prosp. 53, 119991 Moscow, Russia; e-mail: akvonavi@gmail.com;
Yu.V. Kargina, S.A. Shulyapov, I.N. Tsymbalov, R.V. Volkov, V.Yu. Timoshenko Faculty of Physics, Lomonosov Moscow State University, Vorob'evy gory, 119991 Moscow, Russia;
I.V. Bozhev Faculty of Physics, Lomonosov Moscow State University, Vorob'evy gory, 119991 Moscow, Russia; Centre of Quantum Technologies, Moscow State University, Vorob'evy gory, 119991 Moscow, Russia;
A.B. Savel'ev Faculty of Physics, Lomonosov Moscow State University, Vorob'evy gory, 119991 Moscow, Russia; Lebedev Physical Institute, Russian Academy of Sciences, Leninsky prosp. 53, 119991 Moscow, Russia; e-mail: abst@physics.msu.ru

Received 16 March 2021
Kvantovaya Elektronika **51** (6) 536–543 (2021)
Translated by E.N. Ragozin

This work presents the results of complex experimental studies of the effect of the size of structures on the X-ray yield, fast electron generation, and ion acceleration. Femtosecond laser radiation with a peak intensity above 10^{18} W cm^{-2} was focused both on silicon targets with a structure in the form of vertical filaments with characteristic diameters ranging from hundreds of nanometres to several micrometres, and on flat targets. It is demonstrated that all structured targets show an increased absorption of laser radiation in comparison with a flat target. The highest absorption is observed in the case of nanoscale filaments. At the same time, for structured targets an increase was observed in the yield of hard X-ray radiation from the plasma; in this case, targets containing submicron rods demonstrated an increase in the temperature of hot electrons up to 230 keV versus 170 keV for flat targets. The study of fast ions accelerated in plasma has shown that rods with a characteristic diameter of about 1 μm promote an increase in the flux of multiply charged (up to 12+) silicon ions from the plasma, which is supposedly associated with the increased role of collisional ionisation of particles in the plasma.

2. Experimental facility

In the experiments, we used femtosecond radiation from a Ti : sapphire crystal laser with a centre wavelength of 810 nm. The pulse energy on the target was about 20 mJ, the duration was about 55 fs at a repetition rate of 10 Hz. The contrast ratio of the laser pulse relative to the ASE pedestal exceeded 10^9 in 20 ps prior to attainment of the peak intensity. The radiation was focused by an off-axis parabolic mirror onto the target surface at an angle of 45° to the normal (p-polarisation) to a spot with a diameter of about 4 μm at half maximum, the vacuum peak intensity was about 2×10^{18} W cm^{-2}. The setup is shown schematically in Fig. 1.

The following set of techniques was used to diagnose plasma parameters. The optical plasma emission in the direction of the radiation reflected from the target was visualised on a thin white screen, which was imaged onto two CCD cameras equipped with filters that transmitted radiation in the 350–750 nm and 800 ± 20 nm spectral ranges, respectively. To record the spatial distribution of electrons in the direction of reflected radiation, a Lanex scintillation screen was placed at 10 cm from the plasma (behind the screen), additionally protected from optical radiation by an aluminium foil 20 μm thick. The minimum energy of electrons reaching the Lanex screen was ~300 keV. The image from the back side of this screen was transferred by a lens to the third CCD camera. This made it possible to record in each pulse the relative illumination brightness (electron flux) and the angular distribution of electrons (the numerical aperture of the objective constructing the image was equal to 0.4).

The X-ray plasma radiation in the energy range 20–200 keV was recorded by a MediPix array detector on a 1 mm thick CdTe chip (array size: 256 × 256 pixels; pitch: 55 μm). The device was placed at a considerable distance from the plasma so that, on average, one X-ray photon fell on an area of about 10 × 10 pixels per laser pulse, which ensured the measurement of the X-ray radiation spectrum. To record photons with energies above 200 keV, we used a 63-mm thick NaI crystal scintillation detector tuned to the photon count-

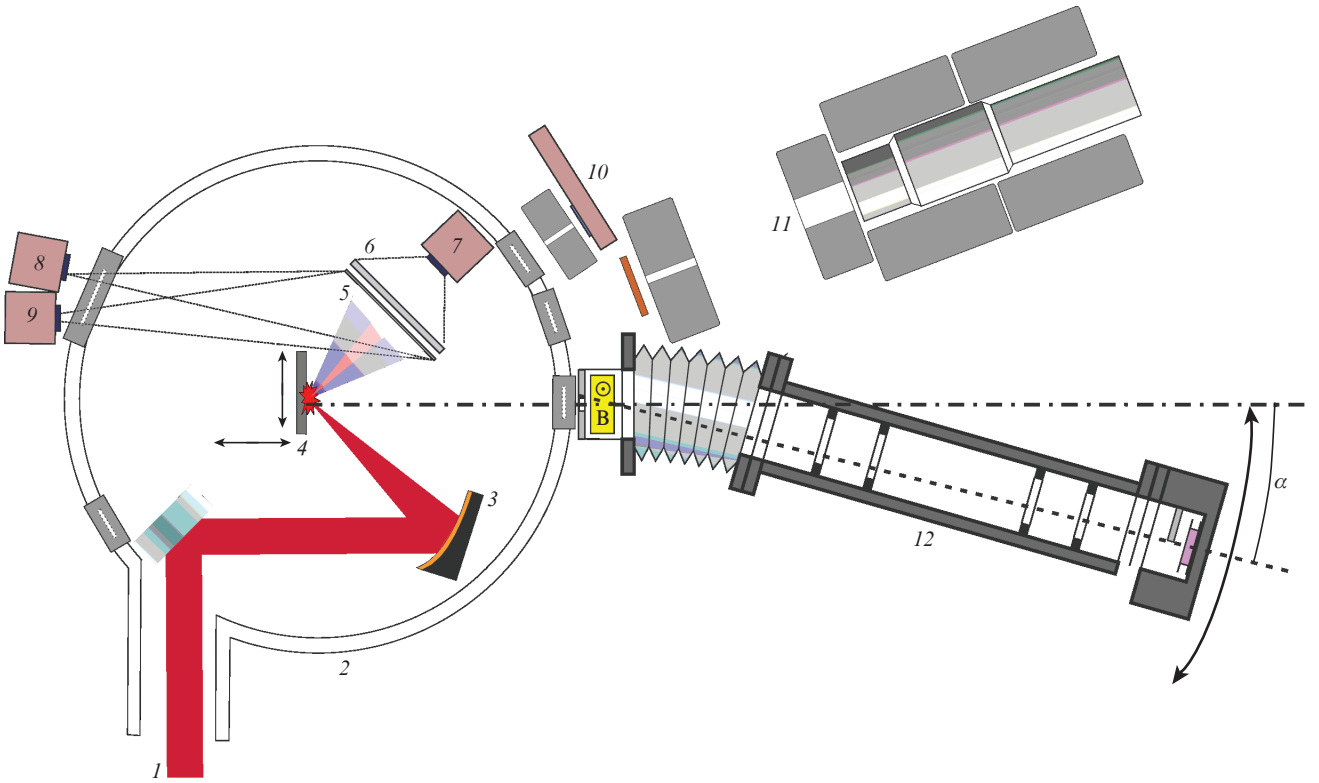

Figure 1. Schematic of the experimental facility:
(*1*) laser pulse; (*2*) vacuum chamber; (*3*) off-axis parabolic mirror; (*4*) target; (*5*) screen for recording optical plasma emission; (*6*) Lanex scintillation screen; (*7*) CCD camera for recording the image of the Lanex plate; (*8*, *9*) CCD cameras of the optical range; (*10*) MediPix X-ray detector; (*11*) scintillation X-ray detector based on NaI crystal; (*12*) time-of-flight ion spectrometer.

ing regime (approximately one photon in three pulses). The energy resolution of both devices was about 10%. X-ray spectra were reconstructed by the Monte Carlo method to take into account the photon scattering in the substance [12].

A time-of-flight ion spectrometer with particle deflection in a constant magnetic field was placed in the direction normal to the target [35, 36]. The length of the time-of-flight base was about 2 m. A permanent magnet (0.15 T) was located near the junction of the vacuum chamber and the time-of-flight tube. A flexible bellows connection allowed the pipe to be deflected through an angle α from 0 to 5° for subsequent identification of particles from charge-to-mass ratio. The ion signal was recorded using a VEU-7 microchannel plate (MCP) (Baspik) of the chevron type and read out with a digital oscilloscope with a 300 MHz bandwidth. The time resolution (about 5 ns) was determined by the response time of the MCP. Accurate measurement of all spectrometer parameters made it possible to reconstruct the energy and charge spectra of particles.

The targets were silicon platelets, smooth or processed by metal-stimulated electrochemical etching [19]. By varying the etching parameters, two samples were obtained with an identical structure – vertical rods or filaments with different (micro- or nanometre) diameters. Figure 2 shows the images of the samples obtained using an electron microscope. By analogy with the abbreviation adopted in the English-language literature, hereinafter the sample with filaments about 100 nm in diameter will be referred to as silicon nanowires (NWs) (Figs 2c and 2d), and the target with micrometre rods as silicon microwires (MWs) (Figs 2a and 2b). Under our interaction conditions, the key difference between the samples is that a greater number of structures fall into the focal spot for the NWs target due to the small diameter of its rods and, in addition, a greater enhancement of the local field near the filament tips can be expected. The MWs target is distinguished by the fact that the radiation is able to penetrate deeper between the rods and heat a thicker surface layer. The height of the rods for the NW target is about 1 μm, while for the MWs it amounts to 10 μm. Changing the etching time makes it possible to control the rod height, which can be important in experiments at a higher radiation intensity, when the radiation can penetrate deep into the structures due to the effect of relativistic transparency. However, in our case, all the main processes occur in the near-surface (up to several hundred nanometres thick) layer, and differences in the height of the columns do not play a role.

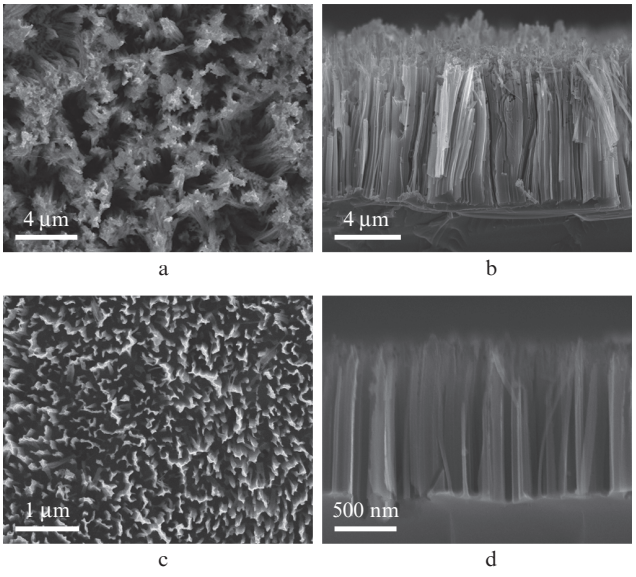

Figure 2. Images of (a, b) MW and (c, d) NW samples obtained with an electron microscope [top (a, c) and side (b, d) view of the sample].

The number of experimental studies comparing targets with structures of different sizes/shapes from the point of view of X-ray production and charged particle acceleration is relatively small [16, 23, 37–39]. Most of the experiments were carried out at moderate intensities [17, 37, 38], or vice versa, lasers with a power of tens and hundreds of terawatts were used [23, 39]. At the same time, laboratory laser-plasma sources with a terawatt peak power of laser radiation, which have a high (over 1 kHz) pulse repetition rate and high stability of parameters, are quite important for applications [40].

3. Experimental results

3.1. Optical plasma emission and hot electron acceleration

Measurement of optical radiation in the direction of reflection of the laser beam with simultaneous detection of fast electrons makes it possible to visually compare the features of its interaction with the target. Figure 3 shows a set of characteristic images obtained from different cameras: the beam reflected from the target surface at a wavelength of $\lambda = 810$ nm (a, d, g), the plasma emission in the optical range 350–750 nm (b, e, h) and the radiation of the Lanex screen (c, f, i).

In the case of flat target irradiation (Figs 3a–3c), the reflected beam has a central core corresponding to specularly reflected radiation and a diffuse component around it. Simultaneously, a beam is generated at the double frequency with a similar divergence (blue glow in Fig. 3b). The source of the second harmonic radiation is the current proportional to the product of the oscillatory velocity of electrons and their density [41]. Therefore, at oblique incidence on the target, the second harmonic beam is generated in the direction of the reflected radiation. The appearance of this frequency in the absence of the red wing in the spectrum of the reflected pulse and of one and a half harmonic radiation indicates a rather sharp ($L/\lambda < 0.1$) plasma boundary due to the high contrast of the laser pulse.

The distribution pattern of the electrons with energies above 300 keV observed on the Lanex screen is generally quite stable from pulse to pulse. The observed distribution is the result of particle acceleration near the critical plasma boundary due to the mechanisms of vacuum heating [42] or ponderomotive acceleration [43], as well as due to the subsequent capture of some of the electrons that escape from the interaction region towards the vacuum by the field of the reflected laser pulse to experience additional direct laser acceleration, whereby the angle of particles emission (cone opening) is determined by the ratio of the longitudinal and transverse momenta [44]. The asymmetry of particle injection associated with oblique incidence leads to the formation of a bright spot on the ring [6, 45]. This sufficiently collimated electron beam does not generate X-ray radiation in the target, since it is formed at a distance from its surface.

In the laser irradiation of the MW target, the resultant patterns varied strongly from pulse to pulse. Obviously, this was due to the commensurability of the structures and the focal irradiation spot, with the result that it was impossible to

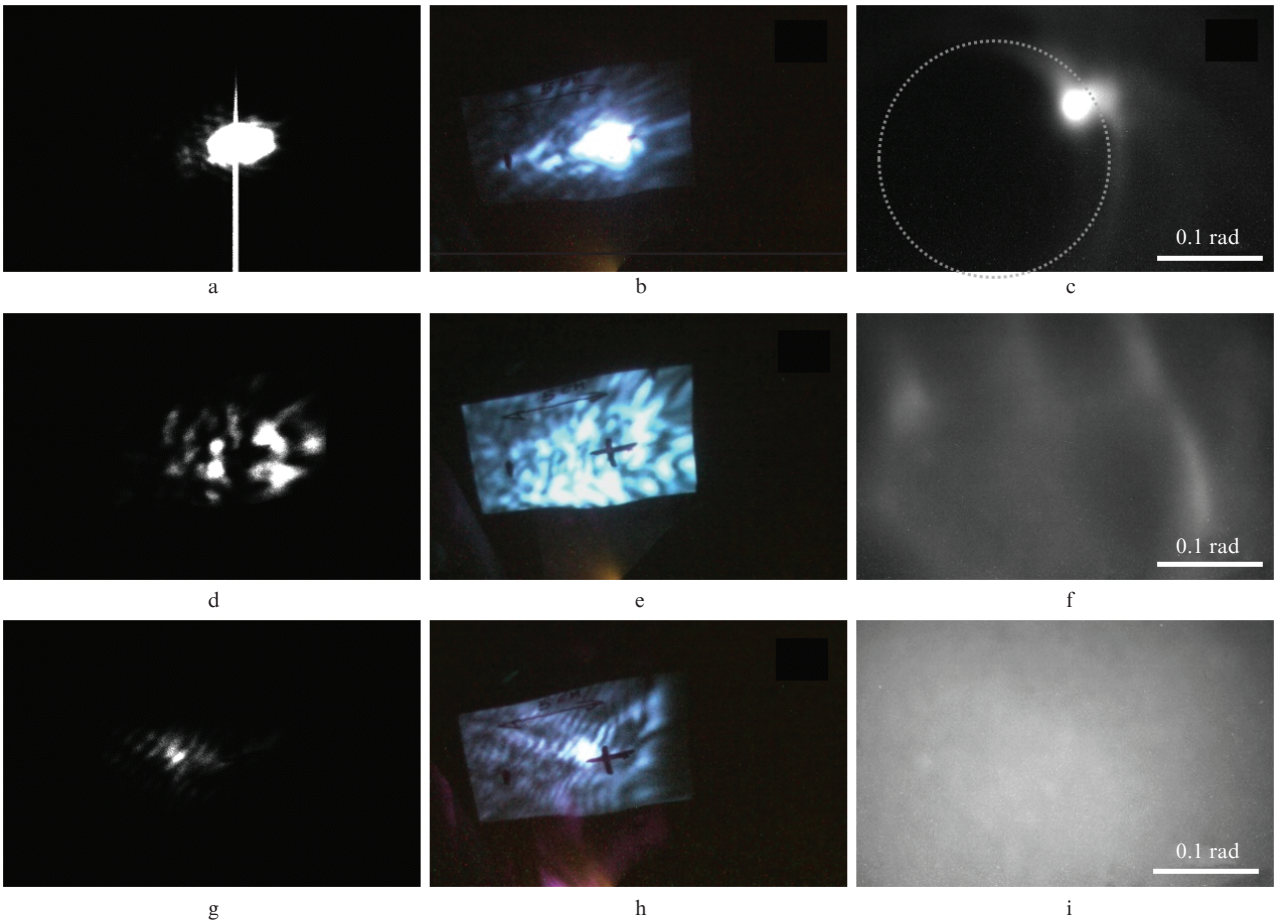

Figure 3. (Colour online) Selection of images obtained from a camera that records (see the facility description) the reflected beam at the carrier wavelength of 810 nm (a, d, g), from a camera that detects plasma emission in the optical range of 350–750 nm (b, e, h), and from the camera to which the image is transferred from the Lanex scintillation screen (c, f, i). The upper row shows the data for a flat sample, the average for the MW target, and the lower row for the NW target.

provide identical experimental conditions. In this case, the images in Figs 3d and 3e have a spotted structure. Each of the spots apparently corresponds to a fairly large fraction of the energy of the incident radiation, since a complex pattern of many electron beams forming a nonuniform ring is also recorded on the Lanex screen (Fig. 3f). In this case, the overall level of illumination of the screen by electrons increased (in comparison with the flat target), which indicates a more efficient absorption of radiation and acceleration of electrons. At the same time, the mechanism of electron acceleration in the case of the MW target is the same as for the flat target. This is due to the large size of the rods: the thickness of each rod exceeds the thickness of the skin layer; therefore, the electrons are vacuum-heated on the surface of each column. However, when radiation penetrates between the columns, the acceleration mechanism can be more complex. It noteworthy that the profile of the target in the interaction region can be reconstructed from the pattern of radiation diffraction at the second or fundamental harmonic [46], but this problem is beyond the scope of this paper.

In the case of an NW target, the intensity of the reflected optical beam is significantly lower (Fig. 3g). In this case, a complex interference pattern can be discerned around the central spot: small variations in the height of the target surface randomly modulate the phase of the reflected radiation; the same is observed at the doubled frequency (Fig. 3h). On the Lanex screen, the pattern is brighter and more uniform than on other targets. We attribute this to the fact that the observed electrons flew directly from the interaction region and did not experience additional acceleration by the field of the reflected pulse. High absorption and the manifestation of such particle acceleration mechanisms as stochastic heating in complex fields [28] increase the number of fast electrons. A sufficiently strong field appears at the rods themselves, from which electrons can be displaced by the laser field throughout their entire thickness (near the vertices, of course, since there are no conditions for the radiation penetration into the depths).

3.2. X-ray measurements

In our case, the main mechanism for hard X-ray generation is the inelastic electron scattering by atoms and ions in a dense target (bremsstrahlung). Figure 4 shows the reconstructed spectra of this radiation obtained by two detectors in the spectral ranges of 20–200 and 200–2000 keV, respectively. Unlike the Lanex plate, which characterises the electrons that leave the target in the direction of the vacuum, X-ray measurements make it possible to determine the parameters of the hot electrons in the path of which the target is located. The exponential slope of the X-ray spectrum is in good agreement with the slope of the electron spectrum [47]; therefore, the

'temperature' of the photon spectrum makes it possible to estimate the 'temperature' of the hot electron component. In Fig. 4, indicated next to the spectra is the temperature of the hot electron component, which corresponds to the slope of the spectrum in this energy range. The grey areas mark the energy ranges in which the reliability of spectrum reconstruction is low.

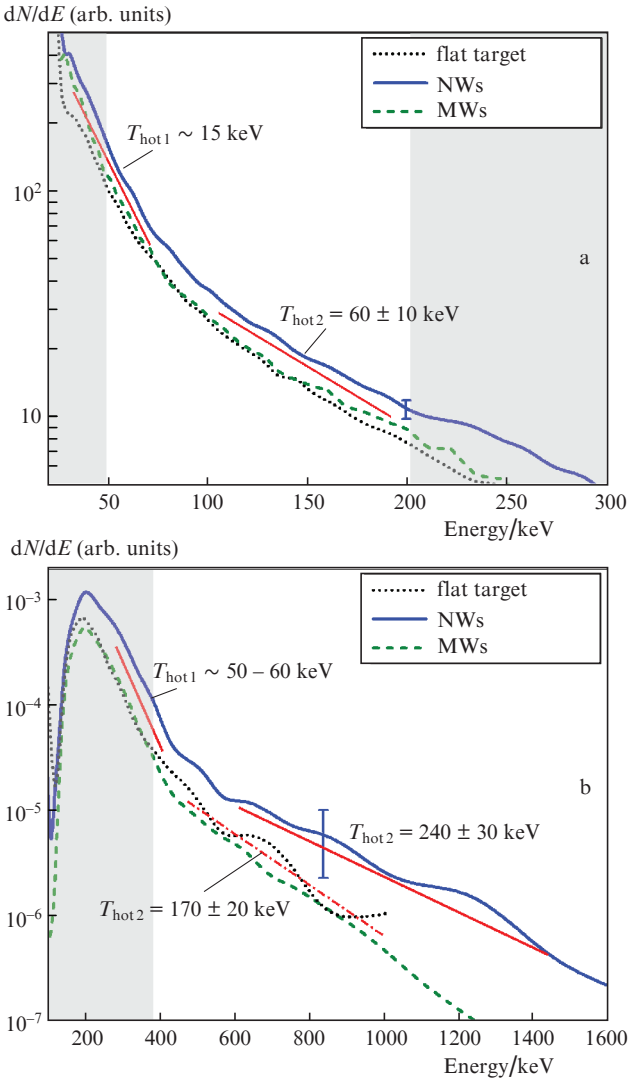

Figure 4. (Colour online) Hard X-ray spectra in the energy range (a) 20–200 keV and (b) over 200 keV. The areas of the spectrum with a low reliability of reconstruction are marked in grey; the red lines show the exponential slope of the spectrum in this area.

In both spectral ranges, it was found that the highest X-rays and gamma-ray flux is achieved with the use of the NW target. This directly reflects the increase in the total number of fast electrons and correlates with the data obtained using the Lanex screen. Compared to the flat sample, the X-ray yield increases by factors of 1.5 and 3 in the ranges of 50–200 keV and over 200 keV, respectively. The photon flux in the range of 20–200 keV for the MW target turned out to be slightly higher than for the flat target; however, in the range above 200 keV, the differences are already minimal. This is probably due to strong signal jumps from pulse to pulse (see above). Since the scintillation detector requires a large number of pulses to obtain a statistically reliable spectrum, the contribution from the more successful shots with a high yield was offset by the contribution of those shots for which the plasma parameters were worse. In the case of the Medipix detector, which records simultaneously many photons in each pulse, the spectra were plotted according to the 100 best realisations in terms of the overall yield of X-ray radiation. Therefore, from the standpoint of making an efficient X-ray source based on a laser with a high pulse repetition rate, a nanostructured target seems to be more promising, since it provides a higher photon yield and a better stability than the microstructured one.

In each of the two spectral ranges, the energy distribution of the photon number dN/dE is close to a two-exponential function of the form $W(E) = A_1\exp(-E/T_{hot1}) + A_2\exp(-E/T_{hot2})$, where $A_{1,2}$ is the amplitude; E is the photon energy; and $T_{hot1,2}$ is the temperature [12]. In the energy range up to 70 keV (Fig. 4a), all three targets have a similar (~15 keV) electron temperature. The estimate uncertainty is high here; however, taking into account this component of the distribution is necessary for correct reconstruction of the spectrum in the region of higher photon energies. In the region above 70–100 keV, the second components are clearly manifested, whose temperatures are also close for different targets and amount to ~60 ± 10 keV. The relative amplitude of this component is approximately 20–30 times smaller, i.e., $A_1/A_2 \approx$ 20–30. The same component (with a temperature of 50–60 keV) is observed in the spectra obtained with a scintillation detector (Fig. 4b) in the region of photon energies below 400 keV.

In the highest-energy part (photon energies above 300 keV, Fig. 4b), the temperature of hot electrons for the flat target and MW one was estimated at 170 ± 30 keV, which is in reasonable agreement with the mechanism of ponderomotive acceleration [43] for the considered value of the peak intensity. It noteworthy that the spectrum for the MW target is averaged over a large number of pulses with significant fluctuations in the parameters; therefore, this estimate does not quite reflect the possible maximum temperature in individual realisations for this target. The temperature for the NW target in this photon energy range turned out to be much higher and amounted to almost 250 keV. In this case, the amplitude of this highest-energy component was approximately 30–40 times lower than the amplitude of the component with a temperature of ~60 keV.

Our analysis suggests that the main mechanisms of laser radiation absorption and electron acceleration in the case of the flat target and the MW one are similar. In the latter case, the interaction area increases, which leads to an increase in the number of fast electrons. In the case of the NW target, not only the number of particles increases, but also their energy. This indicates the appearance of additional mechanisms leading to an increase in the temperature of hot electrons, such as local field enhancement at inhomogeneities and stochastic heating.

3.3. Measurement of ion spectra

A typical form of the signal recorded in one shot and the histogram of the distribution of the ion signal versus the time of arrival, which was plotted after accumulating data for 1000 shots, at a fixed spectrometer deflection angle α are shown in Fig. 5. The instant of detection of UV plasma radiation by the VEU-7 detector is taken as the origin of the time scale. The

smaller the deflection angle α, the higher the amplitude and the longer the decay time of this signal, which makes it difficult to correctly detect the ion signals. This is especially true for protons and highly charged ions, which arrive first. At the same time, of primary interest for this work are silicon ions, whose energy spectra analysis is given below. Since the accumulation of the histogram takes place over a large number of pulses (about one thousand), strongly fluctuating signals are averaged in ion measurements. Numerical calculation of the ion flight in the deflecting magnetic field of the detector, with the inclusion of the edge effects, made it possible to determine the expected time windows of arrival for ions with different nuclear charges and charge states (see Fig. 5). In addition to silicon ions, a significant contribution is made by oxygen ions from the oxide layer [48], as well as by hydrogen and carbon from the surface layer.

The histograms obtained for different deflection angles α make it possible to construct spectra for individual charge states of the silicon ions. In Fig. 6a, these spectra are shown for the flat target, and in Figs 6b–6d they are shown for the three most characteristic silicon charge states obtained for all three samples. It was found that for all targets, ions with a charge less than 8+ (Fig. 6, a) are accelerated by approximately the same field of ~30 keV per charge, which is in reasonable agreement with the temperature of the hot electronic component (~60 keV) previously estimated from X-ray spectra. This signifies that the main contribution to ion acceleration is made not by the energy component with a temperature above 150 keV, but by the component with the greatest number of electrons, whose temperature is approximately the same for all samples. The prevalent charge state for silicon ions is 7+. In this case, the flux of ions with a charge up to 8+ turns out to be approximately the same for all targets (Fig. 6b).

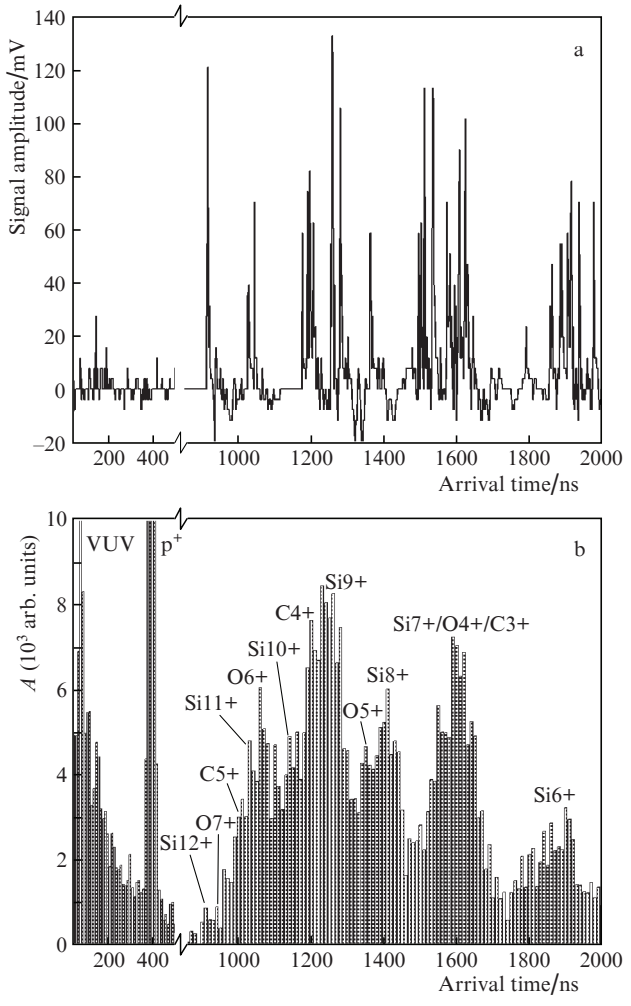

Figure 5. (a) Example of an initial single-shot MCP signal and (b) histogram obtained after adding all the peaks on the TOF spectrometer signal at a fixed deflection angle $\alpha = 1.35°$ and the number of pulses 1000. Different peaks correspond to ions with different charge-to-mass ratios.

At the same time, the efficiency of acceleration of multiply charged ions (11+ and 12+, Figs 6c and 6d, respectively) for the MW target turned out to be significantly higher than for the flat and NW targets, despite the significant error in the spectrum estimate for such charge states due to the small number of recorded particles. Furthermore, the peak in the histogram corresponding to Si12+ partially overlaps with the peak corresponding to O7+. At the same time, the ionization potential of the Si11+ ion (523 eV) is significantly lower than that of the O7+ ion (739 eV) [49]. This gives grounds to believe that the signal observed in the histograms is mainly determined by silicon ions.

To explain the result we arrived at, let us briefly consider the main ionisation processes occurring during the interaction of an ultrashort laser pulse with plasma: ionisation by an electromagnetic field [50], ionisation by an electron impact [51], and ionisation by an ambipolar electron field [52]. The last-named process is rather inherent in the ion acceleration from the reverse side of a thin film, while the first two determine ionisation under our conditions.

The probability of collisional ionisation is proportional to the density of electrons and their temperature. The probability of field above-barrier ionisation increases when the height of the energy barrier suppressed by the field becomes comparable to the ionisation potential. The critical value of the radiation intensity is determined by the expression $I_{\mathrm{BSI}} = 4 \times 10^9 \varepsilon_Z^4/Z^2$ (W cm^{-2}), where ε_Z is the ionisation energy of an ion with a charge $Z-1$ [50]. According to our estimates, a ~50-fs long laser pulse is capable of ionising silicon ions with a high probability to the 8+ state, which is in good agreement with the data on the charge state composition of the plasma. With increasing charge, the probability of field ionisation decreases, and this process is no longer able to provide the production of higher-charge ions in the amount observed in the experiment. Consequently, these ions result from electron impact ionisation [35].

A cloud of hot electrons pulls ions out of the plasma layer, where such electrons are mainly accelerated (near the critical-density region), while the ionisation multiplicity increases as the plasma expands. What leads to an increase in the number of multiply charged ions in the case of an MW target? In our opinion, it is significant that laser radiation generates hot electrons not only at the tips of the rods, but also on their lateral surfaces, since the distance between the rods is comparable to the wavelength of laser radiation. Therefore, the rods, being heated, begin to expand along the target surface, filling in the gaps between them. In this case, ions are accelerated, including from deeper layers of the target (we are talking about hundreds of nanometers), and as they escape towards the surface, they are ionised to higher multiplicities.

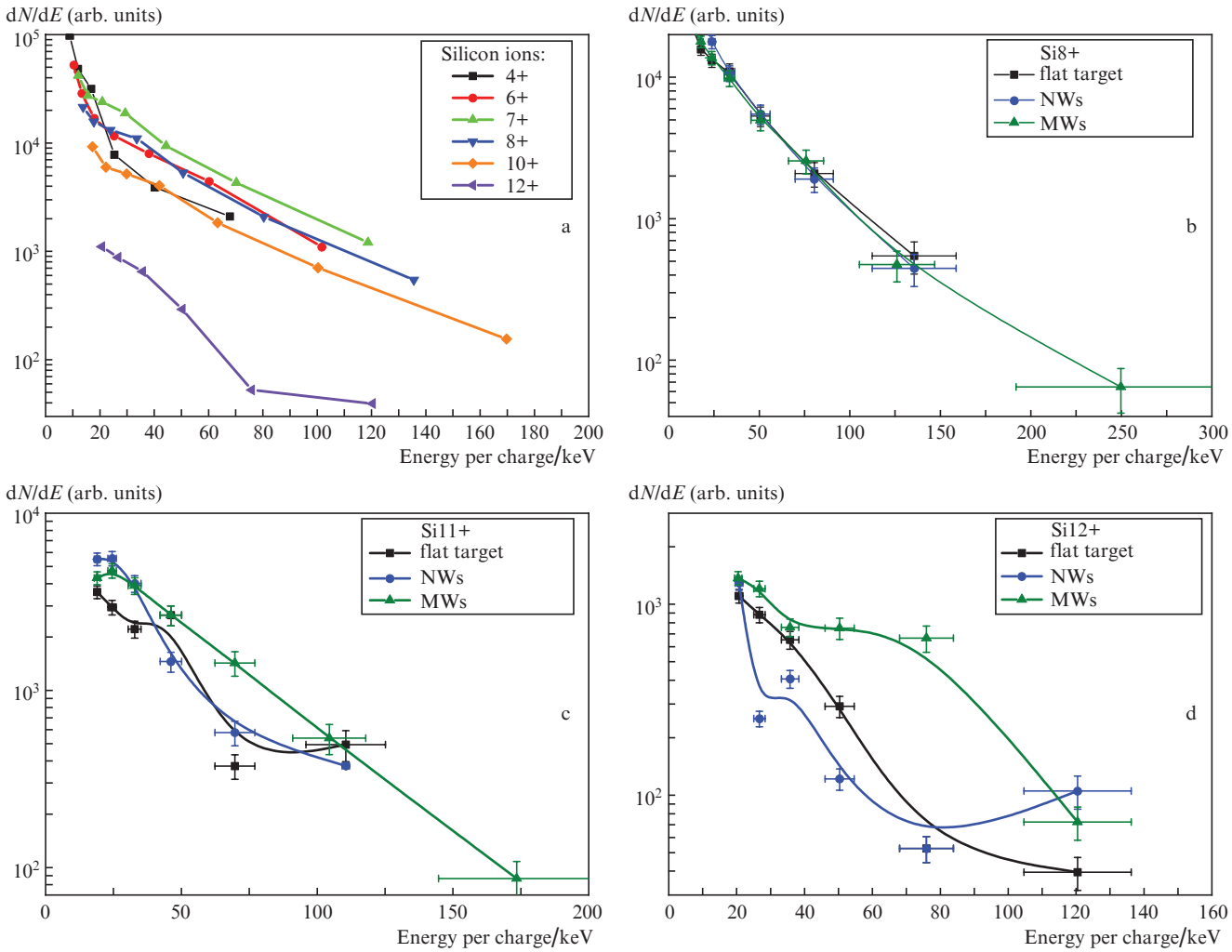

Figure 6. (Colour online) Energy spectra of silicon ions with different charge states for a flat target (a) and spectra of silicon ions with ion charges 8+ (b), 11+ (c), and 12+ (d) for three target samples.

4. Conclusions

In this work, we have experimentally studied the effect of the scale of structures on the target surfaces on the properties of the plasma produced by a femtosecond laser pulse with a peak intensity of 2×10^{18} W cm^{-2}. Two types of silicon rods were investigated: with characteristic rod diameters and spacings of 100 nm and 1 μm, respectively. It is shown that nanoscale rods provide more efficient absorption of laser radiation by plasma: the temperature of the highest-energy electron component rises from 170 keV to almost 250 keV, and the hard X-ray radiation yield increases threefold in comparison with a flat target.

The observed effect is supposedly associated with the more complex dynamics of the electron energy gain when the fields of the laser pulse and ionised rods are combined with an enhancement of the local field at inhomogeneities. Subwavelength-structured targets can be used to create stable X-ray sources.

Irradiation of a target with a micro-structured surface is accompanied by an increase in the flux of multiply charged (11+, 12+) silicon ions from the plasma. More efficient electron impact ionisation occurs due to the penetration of laser radiation between the rods and the acceleration of ions from deeper layers of the target. As the ions escape along the normal, the density of the surrounding thermal electrons increases due to the hydrodynamic expansion of the rods themselves and contributes to an increase in the frequency of electron collisions.

We are currently carrying out additional experimental and numerical studies to provide a more comprehensive interpretation of the observed effects.

It is also important to note that the electrochemical method of etching silicon can provide a wider variety of sizes, diameters, and spacing between the rods. In addition, this method permits preparing large-area samples, which is important for subsequent applications of a laser-produced plasma source with a high pulse-repetition rate.

Acknowledgements. This work was supported by the Russian Science Foundation (Grant No. 18-79-10160). Electron microscopy of the samples was performed using the equipment of the Educational and Methodical Centre for Lithography and Microscopy of Lomonosov Moscow State University.

References

1. Ledingham K.W.D., Galster W. *New J. Phys.*, **12**, 045005 (2010).
2. Mourou G., Tajima T., Bulanov S. *Rev. Mod. Phys.*, **78**, 309 (2006).

3. Barbato F. et al. *Sci. Rep*., **9**, 18805 (2019).
4. Miaja-Avila L. et al. *Struc. Dyn*., **2**, 024301 (2015).
5. Gambari M. et al. *Sci. Rep*., **10**, 6766 (2020).
6. Tsymbalov I. et al. *Plasma Phys. Control. Fusion*, **63**, 022001 (2021).
7. Machi A., Borghesi M., Passoni M. *Rev. Mod. Phys*., **85**, 751 (2013).
8. Ivanov K.A. et al. *Quantum Electron*., **50**, 169 (2020) [*Kvantovaya Elektron*., **50**, 169 (2020)].
9. Andreev A.V., Gordienko V.M., Savel'ev-Trofimov A.B. *Quantum Electron*., **31**, 941 (2001) [*Kvantovaya Elektron*., **31**, 941 (2001)].
10. Park H.-S. et al. *Phys. Plasmas*, **15**, 072705 (2008).
11. Nedorezov V.G., Savel'ev-Trofimov A.B. *Yadernaya Fiz. i Inzhiniring*, **7**, 479 (2016).
12. Ivanov K.A. et al. *Phys. Plasmas*, **21**, 093110 (2014).
13. Jarott L.C. et al. *Phys. Plasmas*, **21**, 031211 (2014).
14. Rosmej O.N. et al. *New J. Phys*., **21**, 043044 (2019).
15. Volkov R.V. et al. *Quantum Electron*., **28**, 1 (1998) [*Kvantovaya Elektron*., **25**, 3 (1998)].
16. Gordienko V.M., Savel'ev-Trofimov A.B. *Phys. Usp*., **42**, 72 (1999) [*Usp. Fiz. Nauk*, **169**, 78 (1999)].
17. Kulcsar G. et al. *Phys. Rev. Lett*., **84**, 5149 (2000).
18. Rajeev P.P. et al. *Opt. Lett*., **29**, 2662 (2004).
19. Ivanov K.A. et al. *Appl. Phys. B*, **123**, 252 (2017).
20. Ebert T. et al. *Phys. Plasmas*, **27**, 043106 (2020).
21. Hu. G.Y. et al. *Phys. Plasmas*, **17**, 13 (2010).
22. Torrisi L. et al. *Phys. Plasmas*, **27**, 043107 (2020).
23. Klimo O. et al. *New J. Phys*., **13**, 053028 (2011).
24. Li H. et al. *Micromech. Microeng*., **27**, 124002 (2017).
25. Vorobyev A.Y., Guo C. *Laser Photon. Rev*., **7**, 385 (2013).
26. Ivanov K.A. et al. *Laser Phys. Lett*., **17**, 045302 (2020).
27. Besozzi E et al. *Nucl. Fusion*, **58**, 036019 (2018).
28. Gozhev D.A. et al. *High Energy Density Phys.*, **37**, 100856 (2020).
29. Andreev A.A. et al. *Plasma Phys. Control. Fusion*, **58**, 14038 (2016).
30. Breizman B.N. et al. *Phys. Plasmas*, **12**, 056706 (2005).
31. Wang W.M., Sheng Z.M., Zhang J. *Phys. Plasmas*, **15**, 030702 (2008).
32. Barsten C. et al. *Sci. Advances*, **3**, e1601558 (2017).
33. Cantono G. et al. *Phys. Plasmas*, **25**, 031907 (2018).
34. Kahaly S. et al. *Phys. Rev. Lett.*, **101**, 145001 (2008).
35. Shulyapov S.A. et al. *Quantum Electron*., **46**, 432 (2016) [*Kvantovaya Elektron*., **46**, 432 (2016)].
36. Mordvintsev I.M., Shulyapov S.A., Savel'ev A.B. *Instrum. Exp. Tech*., **62**, 737 (2019) [*Prib. Tekhn. Eksp*., (6), 11 (2019)].
37. Nikishawa T., Nakano H., Uesugi N. *J. Appl. Phys.*, **96**, 7537 (2004).
38. Mondal S. et al. *Phys. Rev. B*, **83**, 035408 (2011).
39. Sumeruk H.A. et al. *Phys. Plasmas*, **14**, 062704 (2007).
40. Martin L. et al. *High Power Laser Sci., Eng.*, **8**, e18 (2020).
41. von der Linde D., in *Laser Interactions with Atoms, Solids and Plasmas* (Boston, NATO ASI Series (Series B: Physics), 1994) Vol. 327, p. 207.
42. Brunel F. *Phys. Rev. Lett*., **59**, 52 (1987).
43. Wilks S.C. et al. *Phys. Rev. Lett*., **69**, 1383 (1992).
44. Ivanov K.A. et al. *Plasma Phys. Control. Fusion*, **60**, 105011 (2018).
45. Thévenet M. et al. *Nat. Phys*., **12**, 355 (2016).
46. Jarett J. et al. *High Power Laser Sci., Eng*, **7**, e2 (2019).
47. Ivanov K.A. et al. *Contrib. Plasma Phys*., **53**, 116 (2013).
48. Pinilla S. et al. *Phys. Status Solidi (a)*, **213**, 2884 (2016).
49. Grigor'ev I.S., Meilikhov E.Z. (Eds) *Handbook of Physical Quantities* (Boca Raton: CRC Press, 1997; Moscow: Energoatomizdat, 1991).
50. Augst S. et al. *Phys. Rev. Lett*., **63**, 2212 (1989); Delone N.B., Krainov V.P. *Phys. Usp*., **41**, 469 (1998) [*Usp. Fiz. Nauk*, **168**, 531 (1998)].
51. Vainshtein L.A., Sobelman I.I., Yukov E.A. *Excitation of Atoms and Broadening of Spectral Lines* (Berlin, N.Y.: Springer, 1981, 1995; Moscow: Nauka, 1979).
52. Hegelich M. et al. *Phys. Rev. Lett*., **89**, 085002 (2002).